Reviews of Electromagnetics, Vol. IV, 2025
EuCAP 2025 Special Issue
DOI: 10.53792/RoE/2025/25021

Reviews of Electromagnetics
EuCAP 2025 Special Issue

Performance Analysis for the Near Field Partial Characterization Approach for Aperture Antennas

Amedeo Capozzoli*, Claudio Curcio, Angelo Liseno

Abstract
In the framework of Near-Field Characterization a new approach has been recently proposed, devoted to the so called Partial Characterization: its aim is to retrieve the Far-Field pattern along some cuts only, by using a proper set of Near-Field data, "reduced", with respect to the one adopted in the standard characterization approaches. In this paper a detailed analysis highlighting the capabilities of the approach is reported.

Key terms
near-field antenna characterization; partial characterization

Dipartimento di Ingegneria Elettrica e delle Tecnologie dell'Informazione
***Corresponding author**: a.capozzoli@unina.it

Received: 14/07/2025, Accepted: 24/12/2025, Published: 30/12/2025

1. Introduction

The reduction of the measurement time in Near-Field antenna measurements is a relevant issue and can be achieved following several directions. The main route is to exploit some (more or less weak) a-priori information about the Antenna Under Test (AUT) to reduce the number of NF samples and/or the scanning path length [1–3]. Another option is represented by acquisition systems equipped with multi-probes [4]. In both cases, the standard characterization is typically considered, aimed at reconstructing the whole Far-Field Pattern (FFP) of the Antenna Under Test (AUT), i.e. Whole Characterization (WC) methods.

On the other hand, in some cases of interest in the applications, just some features of the radiator/scatterer electromagnetic behaviour are relevant for the end user, as in the case of phased arrays or base station antennas, wherein only cuts of the FFP are sufficient [5–7], or when dealing with the testing of antennas manufactured in series. Accordingly, opposite to WC, Partial Characterization (PC) [5–13] approaches have been proposed, whose aim is to reconstruct the FFP just along the cuts of interest. The advantage of PC is the expected drastic reduction of the NF data needed by the post processing algorithm turning the Near-Field information into the Far-Field reconstruction, if compared to WC approaches, which should correspond a drastic reduction of the measurement acquisition time.

In [10], a general mathematical framework for PC has been introduced. Given the goals of the desired PC, the approach defines the optimal distribution of the NF samples after exploiting some weak information about the scatterer/radiator. In addition, also bounds are provided to the expected reconstruction error due to the reduced amount of collected data in the NF.

An extensive numerical as well as experimental analysis has been carried out to validate the approach [10]. In [11] the behavior of the error bound as a function of the measurement parameters has been preliminarily discussed, supported by some experimental results too. Here, a more detailed analysis is presented, which highlights the capabilities of the approach.

To introduce the approach, let us clarify that the goal is achieved thanks to two key features:

a) The formulation of the NF characterization as a linear inverse problem;

b) The use of Singular Value Optimization (SVO) to determine the optimal NF samples distribution.

Points a) and b) are summarized in Section II, while Section III describes the method in some details. The numerical results are then discussed in Section IV.

2. Formulation of the NF Characterization

The approach is described with reference to planar aperture antennas and planar scanning geometry. However, it can be extended to more general geometries and to the case of scatterers characterization instead of antenna characterization.

The AUT is represented by a rectangular aperture $\mathscr{D}_{ap}$, $2a_{ap} \times 2b_{ap}$ sized, centred in the Oxyz reference system (Fig. 1).

The NF radiation operator $\mathscr{T}$ links the aperture field to the NF over the scanning plane. In particular, it maps the aperture field to measured field on the measurement domain $\mathscr{D}$, a rectangular region, $2a \times 2b$ sized, located in the $z=d$ plane (see Fig. 1). In its general form, the selected expression for $\mathscr{T}$ can, obviously, account for the probe response to compensate its effect on the characterization process.

The final goal of the characterization is the evaluation of the FFP along the cuts of interest from the retrieved aperture field. To this end, a second operator, the radiation operator $\mathscr{R}$, is introduced, mapping the aperture field to the FFP along the desired observation directions.

Obviously, the operator $\mathscr{T}$ has functional nature. To handle it numerically, its discrete counterpart is considered after representing its inputs and outputs with their finite-dimensional counterparts, belonging to finite-dimensional linear subspaces, properly selected to control the approximation error:

- a finite number Q of measurements points for the measurement field, so that the measurement field is represented by a Q-sized vector $\underline{b}$, belonging to the linear finite dimensional subspace $\mathscr{B}$;
- a finite number of P expansion coefficients of the aperture field with respect to a proper set of basis functions, so that the aperture field is described by the P-sized vector $\underline{a}$, belonging to the linear finite dimensional subspace $\mathscr{A}$;

For the case of aperture antennas, we represent the aperture field by means of Prolate Spheroidal Wave Functions with space-bandwidth product accounting for the spatial and spectral support of the aperture field [2, 10, 14].

Accordingly, $\underline{a}$ and $\underline{b}$ are related each other by means of a QxP sized matrix, say $\underline{\underline{T}}$, representing $\mathscr{T}$:

$$\underline{\underline{T}} \cdot \underline{a} = \underline{b} \tag{1}$$

In the same way, after considering a finite number L of observation directions, the FFP can be described by using the L-sized vector $\underline{f}$, and the Far-Field radiation operator can be accounted for by introducing its discrete counterpart:

$$\underline{\underline{R}} \cdot \underline{a} = \underline{f} \tag{2}$$

where $\underline{\underline{R}}$ is a LxP sized matrix.

The NF-characterization amounts to retrieve $\underline{a}$ from $\underline{b}$ thanks to a regularized inversion of Eq. 1, and then evaluate $\underline{f}$ after Eq. 2 [2, 10, 14].

Equation 1 is, clearly, dependent on the peculiar distribution of the measurement points. A non-uniform distribution can be adopted reduce the number of the measurement locations, without impairing the reconstruction of $\underline{f}$. SVO technique can be adopted to define the optimal samples distribution [2, 10, 14].

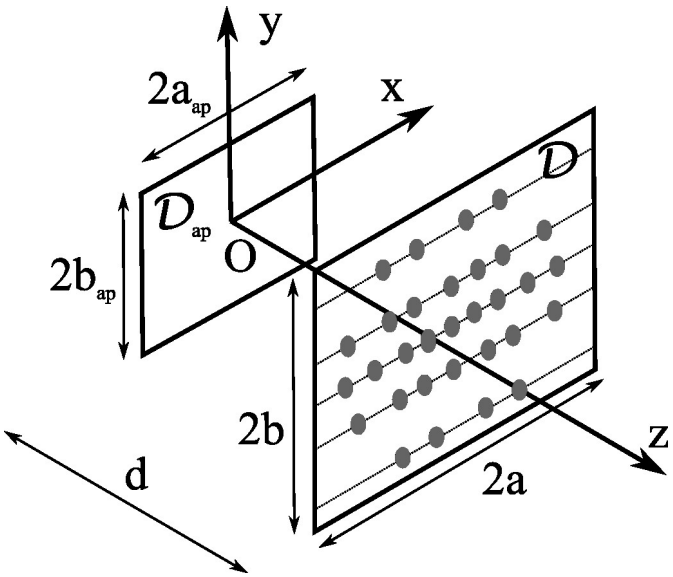

Figure 1: Geometry of the problem.

SVO is based on the idea that the optimal spatial distribution of the measurement points should be the one optimizing the behaviour of the singular values of the relevant linear operator, according to a proper metric [15].

Thanks to an optimization procedure, SVO is able to determine the optimal number and distribution of the measurement samples, with a drastic reduction of the number of acquisition points and scanning path length with respect to standard as well as optimized sampling schemes. For WC, the effectiveness and the accuracy of the reconstruction attainable with the SVO measurement "grid" have been experimentally verified in different measurement geometries [2, 14–16].

3. The PC Approach

To introduce PC, a graphical comparison of the observation directions for WC and PC is presented in Fig. 2, wherein their locations are depicted as black circles. In the WC case, the observation directions span, in principle, the whole visible domain, and the value of L can be quite large. On the contrary, for PC, the worked example accounts for one cut only of the FFP (in the picture the horizontal principal cut is showed, even if others can be adopted), so that the value of L can be significantly smaller than that of WC. In Fig. 2 the patterns are depicted as functions of the cosine directors u and v, related to the spherical coordinates θ and ϕ by $u = \sin\theta\cos\phi$ and $v = \sin\theta\sin\phi$.

After considering the singular value decomposition of $\underline{\underline{R}}$, and after defining P_1 as the number of relevant singular values of $\underline{\underline{R}}$, it can be seen that:

- for the PC, P_1 can be smaller than P;
- the subspace $\mathscr{A}$ can be segmented into the direct sum of two subspaces $\mathscr{A}_1$ and $\mathscr{A}_2$, one orthogonal to each other, as schematically depicted in Fig. 3a;
- $\mathscr{A}$ has size equal to P, while $\mathscr{A}_1$ and $\mathscr{A}_2$ have sizes equal to P_1 and P-P_1, respectively;

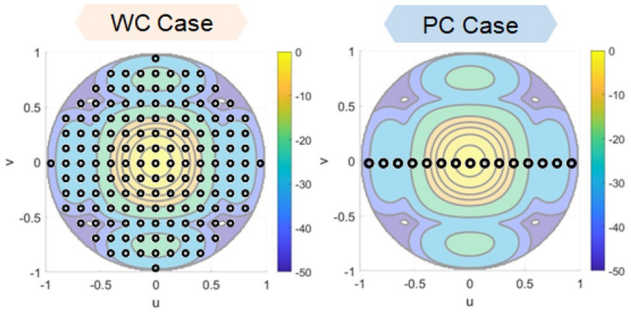

Figure 2: Locations of the observation directions in the visible domain: comparison between WC and PC.

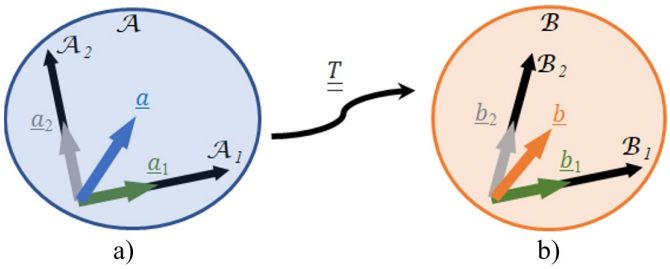

Figure 3: Spaces involved in the PC: a) Segmentation of $\mathscr{A}$; b) Segmentation of $\mathscr{B}$.

- each vector $\underline{a}$ can be written as $\underline{a} = \underline{a}_1 + \underline{a}_2$, where $\underline{a}_1 \in \mathscr{A}_1$ is useful to reconstruct the FFP along the cut of interest, while $\underline{a}_2 \in \mathscr{A}_2$ does not.

Thanks to $\underline{\underline{T}}$, also $\underline{b}$ can be written as the sum of a term useful to PC, say $\underline{b}_1$, and an undesired term, say $\underline{b}_2$ (see the scheme in Fig. 3b).

The first step of the PC processing is to retrieve only $\underline{a}_1$ starting from the whole NF data vector $\underline{b}$. Unfortunately, since $\underline{b}_1$ and $\underline{b}_2$ are not orthogonal each other, a criterion is needed to define the optimal distribution of measurement allowing the two goals:

G1 The stable extraction of $\underline{b}_1$ from $\underline{b}$.

G2 The reliable inversion of $\underline{a}_1$ from $\underline{b}_1$.

The solution strategy is schematically depicted in the flow chart showed in Fig. 4. The final distribution of the measurement points is obtained as the union of two different distributions, D1 and D2. When the effects of $\underline{b}_2$ are negligible, the problem reduces to G2 only, fulfilled by D1. On the contrary, when the presence of $\underline{b}_2$ is relevant, further measurement samples are needed to realize the task G1, thanks to the distribution D2.

For D1, an estimate for the error bound on the FFP, say $\varepsilon_{\max}$, due to the presence of $\underline{b}_2$ can be derived, by exploiting some a-priori information on the radiator. Accordingly, after defining the maximum tolerable error on the FFP, say ε_0, PC can be performed according the scheme in Fig. 4. Indeed, after D1 is obtained, $\varepsilon_{\max}$ is available. Accordingly, if $\varepsilon_{\max} < \varepsilon_0$, PC

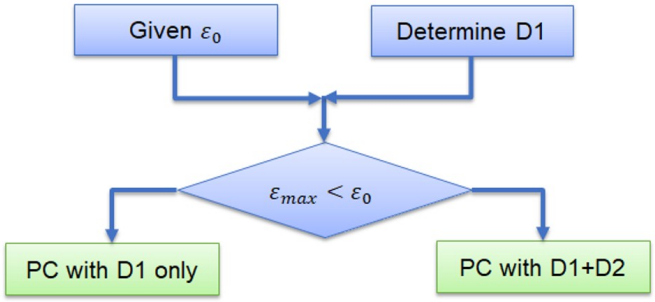

Figure 4: Flow Chart of the PC strategy.

can be performed from D1 only. On the contrary, D2 samples are mandatory to control the reconstruction error.

A deep discussion about the determination of D1 and D2 is reported in [10]. Here the attention is focused on the behaviour of the reconstruction error. Hence, just a short summary is reported.

In the limit case $\underline{b}_2 = 0$, Eq. 1 turns into:

$$\underline{b}_1 = \underline{\underline{T}} \cdot \underline{a}_1, \qquad \underline{a}_1 \in \mathscr{A}_1 \tag{3}$$

To determine D1 SVO is applied to the problem in eq. 3. It is worth noting that, since $\underline{a}_1$ belongs to a P_1-sized linear subspace, the inverse problem in Eq. 3 involves only P_1 unknowns.

On the other hand, the FFP vector $\underline{f}$ can be linked to $\underline{b}_1$ by using:

$$\underline{\underline{S}}_1 \cdot \underline{f} = \underline{b}_1, \tag{4}$$

where, after defining:

- $\underline{\underline{V}}_{\mathrm{R}}$ as the matrix containing the right singular vector of $\underline{\underline{R}}$;
- $\underline{\underline{V}}_{\mathrm{R1}}$ as the matrix given by the first P_1 columns of $\underline{\underline{R}}$;
- $\underline{\underline{R}}_1 = \underline{\underline{R}} \cdot \underline{\underline{V}}_{\mathrm{R1}}$ and $\underline{\underline{R}}_1^{\dagger}$ as the pseudoinverse of $\underline{\underline{R}}_1$;
- $\underline{\underline{T}}_1 = \underline{\underline{T}} \cdot \underline{\underline{R1}}$

the matrix $\underline{\underline{S}}_1$ is given by:

$$\underline{\underline{S}}_1 = \underline{\underline{T}}_1 \cdot \underline{\underline{R}}_1^{\dagger}, \tag{5}$$

Actually, $\underline{b}_2$ can be seen like a "noise" additive term affecting the inversion of $\underline{f}$ in Eq. 5. Accordingly, if an estimate, in norm, of the effects of $\underline{b}_2$ with respect to $\underline{b}_1$, is available, the error bound $\varepsilon_{\max}$ on the reconstruction of the FFP can be obtained as:

$$\frac{\|\delta \underline{f}\|}{\|\underline{f}\|} \leq \mathrm{cond}\left(\underline{\underline{S}}_1\right) \frac{\|\underline{\underline{P}}_1 \cdot \underline{b}_2\|}{\|\underline{b}_1\|} = \mathrm{cond}\left(\underline{\underline{S}}_1\right) \rho = \varepsilon_{\max} \tag{6}$$

where

- $\delta \underline{f}$ is the error term with respect to the nominal FFP;
- $\underline{\underline{P}}_1 = \underline{\underline{U}}_1 \cdot \underline{\underline{U}}_1^H$, $\underline{\underline{U}}_1$ being the matrix containing the relevant left singular vectors of $\underline{\underline{T}}_1$;

- $\|\cdot\|$ denotes the ℓ^2 norm, and the apex H stands for Hermitian conjugate;
- cond$(\cdot)$ represents the condition number of the matrix at hand;
- $\rho = \|\underline{\underline{P}}_1 \cdot \underline{b}_2\| / \|\underline{b}_1\|$ is the cited measure of the effects of $\underline{b}_2$ on the inversion.

The parameter ρ could be estimated by exploiting some, even weak, a priori information about the radiator [10].

4. Numerical Analysis

The proposed PC approach has been numerically and experimentally validated with realistic antenna cases in [10, 11]. In [11], the behavior of $\varepsilon_{\max}$ as function of the measurement distance d has been analyzed, for canonical square apertures with different sizes. As discussed before, $\varepsilon_{\max}$ is the bound for the reconstruction error on the FFP achievable when using only D1: as long as this bound is acceptable, PC can be performed in the fastest way, without adding the further points of D2.

In this paper the attention is focused on the reconstruction error achievable when using the D1 only. As study cases, square apertures with different sizes are considered, and PC is performed by using data collected for different d values. Firstly, uniformly illuminated apertures are examined, and the reconstructed FFP along the cut of interest is shown, together with the reconstruction error. Then, the case of a non-separable illumination is considered, to analyze how the reconstruction error changes according to the parameters, with respect to the previous case. For one case, the improvement due to the use of the D2 is discussed. Finally, the case of a non-canonical radiator is presented.

For all the worked cases, the aperture field is assumed linearly polarized along the x-axis.

Two different aperture sizes are considered: $6\lambda \times 6\lambda$ (Case 1) and $12\lambda \times 12\lambda$ (Case 2). For all the worked cases, the PC along the cut *v=0* cut is considered, and three values for d are analysed: $5\lambda, 10\lambda$ and 15λ.

In Fig. 5 the distributions D1 obtained for the different values of d in Case 1 are reported: these involve 19, 25 and 33 non uniformly spaced field samples, for d equal to $5\lambda, 10\lambda$ and 15λ, respectively. In Fig. 6, the three distributions D1 in Case 2 are shown: in this case 51, 49 and 55 filed samples are required for the three distances.

As shown in the Figs. 5- 6 the extent of the D1 region increases as the measurement distance increases. Accordingly, SVO is able to control automatically the truncation error [12]. it can be seen the extent of D1 is enlarged as the measurement distance increases. In this way the SVO allows to mitigate the truncation error as a longer measurement distance is taken into account [17].

The NF data radiated by the apertures have been collected at the sampling points and exploited to reconstruct the relevant component of the FFP along the cut of interest.

In the case of uniform illumination decreases as d increases, from about 80% for the shorter distance, to 26% (Case 1) and 23% (Case 2) for $d=15\lambda$.

The number of samples Q and the obtained for a uniform illumination applied to both aperture cases are summarized in Tab. 1 (rows #1 to #6)

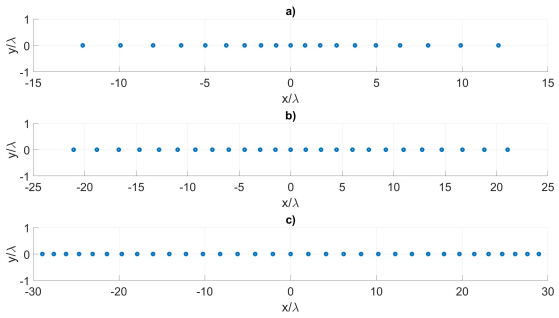

Figure 5: Sampling points for D1 – Case 1: a) $d = 5\lambda$, b) $d = 10\lambda$, c) $d = 15\lambda$.

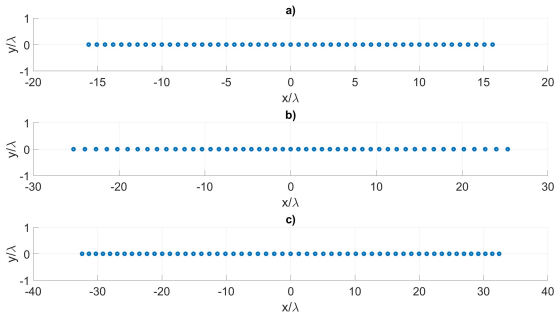

Figure 6: Sampling points for D1 – Case 2: a) $d = 5\lambda$, b) $d = 10\lambda$, c) $d = 15\lambda$.

The corresponding FFP are reported in Figs. 7- 9 for the three distances, for Case 1, and in Figs. 10- 12 for Case 2. The Patterns (blue line) are compared with the numerical reference (red stars): the relative reconstruction error is reported too, as a black dashed line. As it can be clearly appreciated, the reconstruction error follows the same trend of $\varepsilon_{\max}$: a larger reconstruction error is obtained for shorter values of d, while longer measurement distances allows an improved reconstruction. If one retains as acceptable a relative error not greater than -40dB, good performance are achieved in all these cases. In any case the reconstruction error can be further improved, but the D2 distribution is required.

To highlight the effects of noise, but to let the Reader appreciate the error of PC, noise has been considered just in Case 1), for $d=15\lambda$. An independent and normally distributed random contribution has been added, for three Signal to Noise Ratio (SNR) levels, equal to 40dB, 30dB and 20dB. The corresponding reconstructions are reported in Figs. 13- 15. The results show a good stability of the FFP prediction, with an error coherent with the considered SNR.

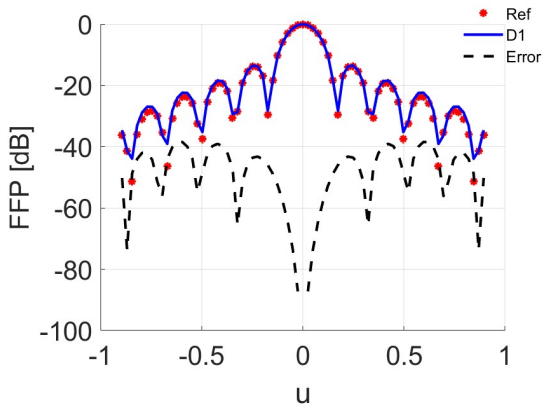

Figure 7: Reference FFP (red crosses), FFP reconstructed with D1 (blue line) and relative reconstruction error (black dashed line): PC along the cut for $v=0$, uniform illumination, Case 1 - $d=5\lambda$.

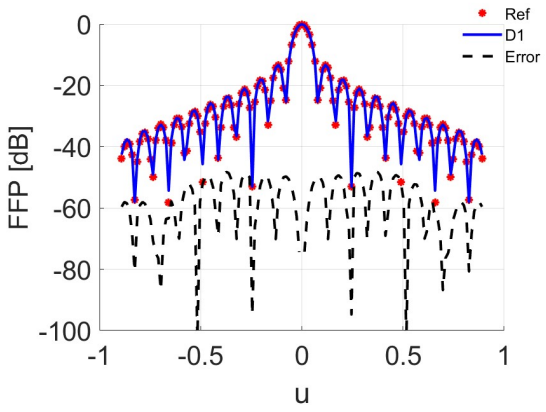

Figure 10: Reference FFP (red crosses), FFP reconstructed with D1 (blue line) and relative reconstruction error (black dashed line): PC along the cut for $v=0$, uniform illumination, Case 2 - $d=5\lambda$.

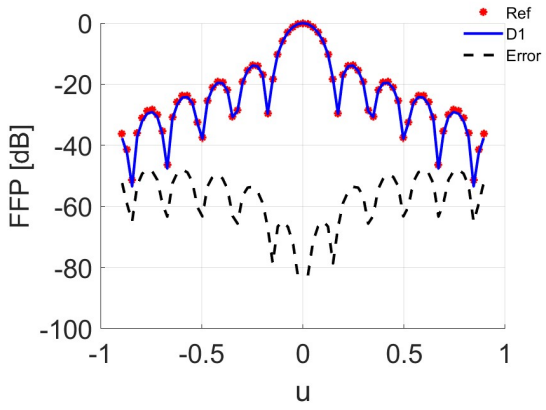

Figure 8: Reference FFP (red crosses), FFP reconstructed with D1 (blue line) and relative reconstruction error (black dashed line): PC along the cut for $v=0$, uniform illumination, Case 1 - $d=10\lambda$.

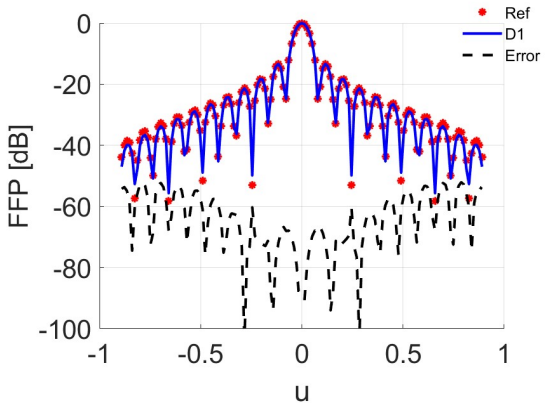

Figure 11: Reference FFP (red crosses), FFP reconstructed with D1 (blue line) and relative reconstruction error (black dashed line): PC along the cut for $v=0$, uniform illumination, Case 2 - $d=10\lambda$.

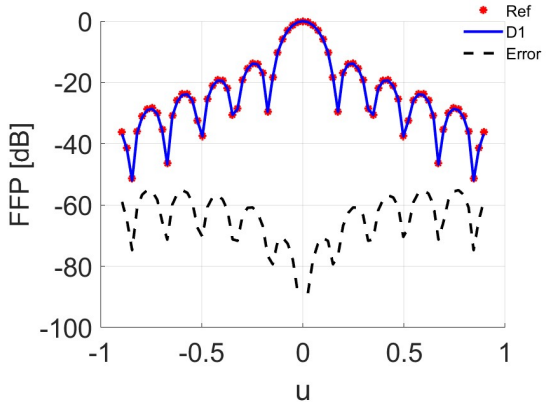

Figure 9: Reference FFP (red crosses), FFP reconstructed with D1 (blue line) and relative reconstruction error (black dashed line): PC along the cut for $v=0$, uniform illumination, Case 1 - $d=15\lambda$.

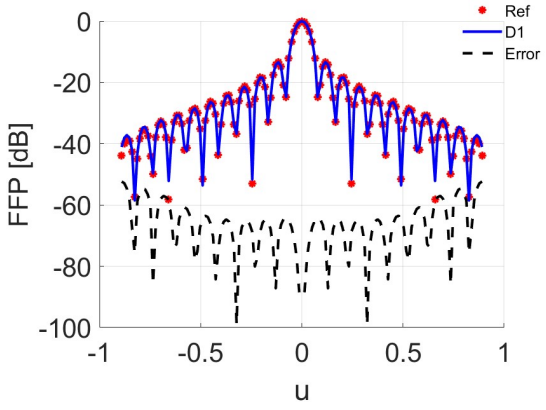

Figure 12: Reference FFP (red crosses), FFP reconstructed with D1 (blue line) and relative reconstruction error (black dashed line): PC along the cut for $v=0$, uniform illumination, Case 2 - $d=15\lambda$.

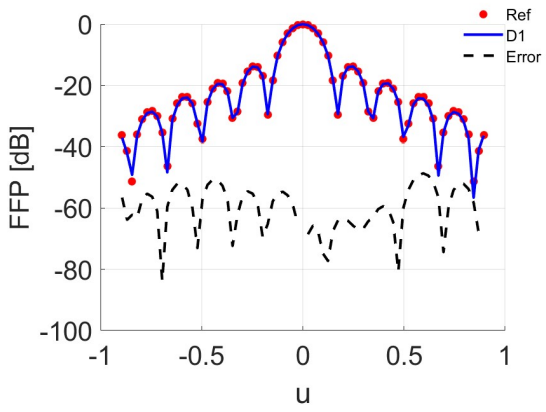

Figure 13: Reference FFP (red crosses), FFP reconstructed with D1 (blue line) and relative reconstruction error (black dashed line): PC along the cut for *v=0*, uniform illumination, Case 1 - *d=15λ* - *SNR=40dB*.

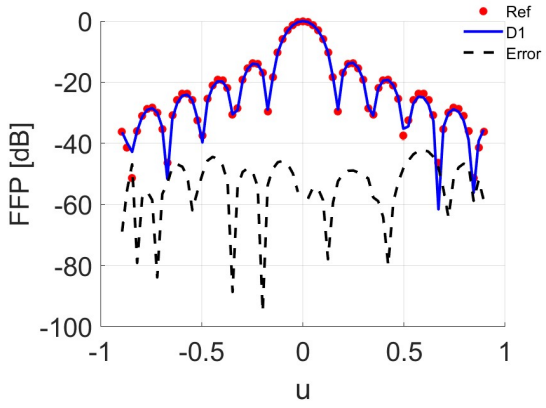

Figure 14: Reference FFP (red crosses), FFP reconstructed with D1 (blue line) and relative reconstruction error (black dashed line): PC along the cut for *v=0*, uniform illumination, Case 1 - *d=15λ* - *SNR=30dB*.

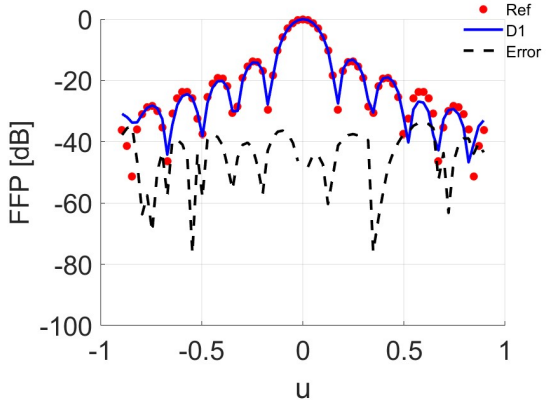

Figure 15: Reference FFP (red crosses), FFP reconstructed with D1 (blue line) and relative reconstruction error (black dashed line): PC along the cut for *v=0*, uniform illumination, Case 1 - *d=15λ* - *SNR=20dB*.

Regarding the non-separable excitation, an exponential circular tapering of 10dB has been adopted [10]. For this excitation, ε_{max} is greater than 100%, when $d=5\lambda$, and reduces up to about 42% for $d=15\lambda$, while for Case 2, ε_{max} is greater than 200% for $d=5\lambda$ and $d=10\lambda$ and about 58% for $d=15\lambda$. As for the case of uniform illumination, the results are summarized in Tab. 1 (rows #7 to #12).

Table 1: Results Summary

#	Case	Illumination	d	Q	ε_{max}
1			5λ	19	78%
2	1	Uniform	10λ	25	44%
3			15λ	33	26%
4			5λ	51	85%
5	2	Uniform	10λ	49	79%
6			15λ	55	23%
7			5λ	19	115%
8	1	Tapered	10λ	25	70%
9			15λ	33	42%
10			5λ	51	244%
11	2	Tapered	10λ	49	222%
12			15λ	55	58%

Case 2 – D1 + D2

#	Case	Illumination	d	Q–$D1$	Q–$D2$	Q–HW
13	2	Tapered	5λ	51	676	6561

The corresponding results for Case 1) are reported in Figs. 16- 18, while those for Case 2 in Figs. 19- 21. For Case 1, the reconstruction error follows the same trend of ε_{max} as a function of d and the reconstruction error remains at the same level of the uniform illumination. In Case 2, the reconstruction error is larger and the -40dB error requirement is not satisfied, as also suggested by the ε_{max} values, and the distribution D2 is required.

Indeed, let us show how D2 can improve the reconstruction error, for Case 2, $d=5\lambda$ and the non-separable illumination. In Fig. 22 the final distribution is reported: D2 (blue circles) is made of 26 non-uniformly spaced rows, made of 26 samples each, non-uniformly spaced along the x-axis, with a minimum spacing between two adjacent sampling points greater than 0.7λ. In Fig. 23 the results achievable by using also D2 are reported, for the case of the non-separable source: as it can be seen the reconstruction error is dramatically reduced, by using only further 676 samples. Regarding the estimate of the reconstruction quality, the FFP obtained with the PC has been compared with the numerical reference, while, regarding the estimate of the measurement time it is useful to compare the distribution of the sampling points obtained provided by the PC with the standard measurement grid adopted for the WC case. In particular, a rough estimate of the time saving of PC with respect to WC can be obtained by comparing the number of

rows: if a standard half-wavelength sampling over a $40\lambda \times 40\lambda$ grid, is adopted for WC, the PC measurement time would be, in this case, at least, equal to 27/81 of that of WC. In Tab. 1, row #13, the number of samples required for both D1 and D2 are reported as Q-D1 and Q-D2, respectively, together with the number of samples Q-HW required for the cited standard half-wavelength grid.

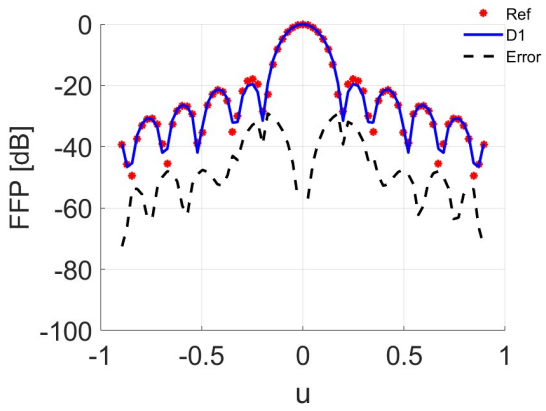

Figure 16: Reference FFP (red crosses), FFP reconstructed with D1 (blue line) and relative reconstruction error (black dashed line): PC along the cut for *v=0*, non-separable illumination, Case 1 - $d=5\lambda$.

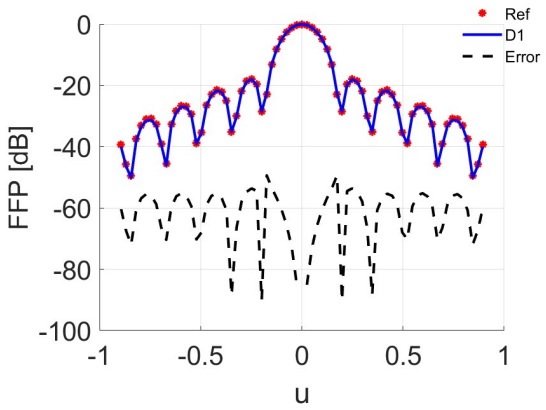

Figure 18: Reference FFP (red crosses), FFP reconstructed with D1 (blue line) and relative reconstruction error (black dashed line): PC along the cut for *v=0*, non-separable illumination, Case 1 - $d=15\lambda$.

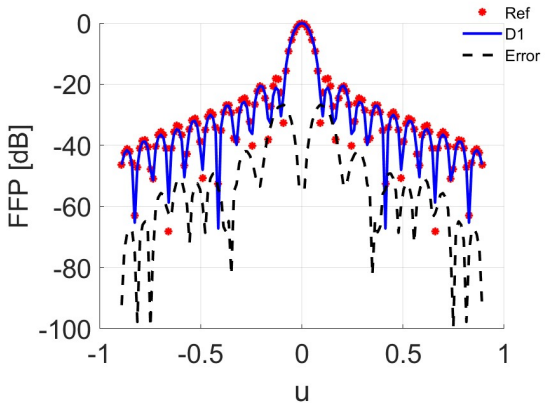

Figure 19: Reference FFP (red crosses), FFP reconstructed with D1 (blue line) and relative reconstruction error (black dashed line): PC along the cut for *v=0*, non-separable illumination, Case 2 - $d=5\lambda$.

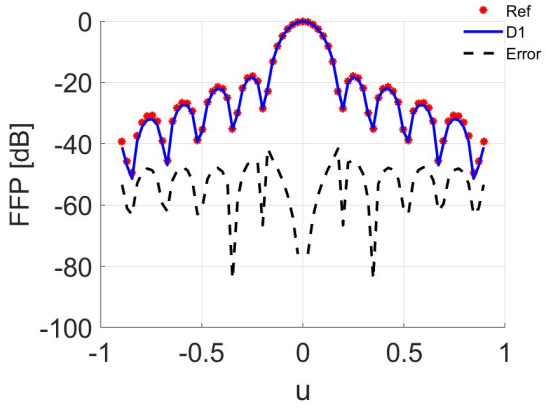

Figure 17: Reference FFP (red crosses), FFP reconstructed with D1 (blue line) and relative reconstruction error (black dashed line): PC along the cut for *v=0*, non-separable illumination, Case 1 - $d=10\lambda$.

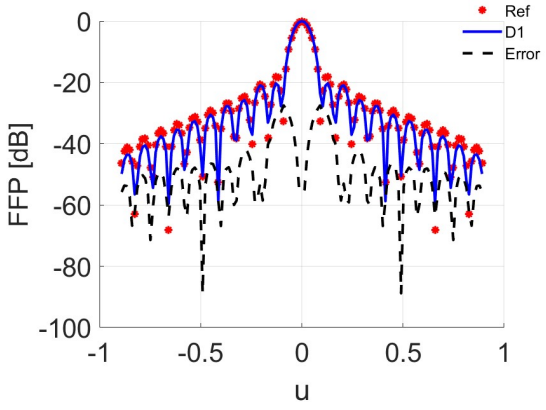

Figure 20: Reference FFP (red crosses), FFP reconstructed with D1 (blue line) and relative reconstruction error (black dashed line): PC along the cut for *v=0*, non-separable illumination, Case 2 - $d=10\lambda$.

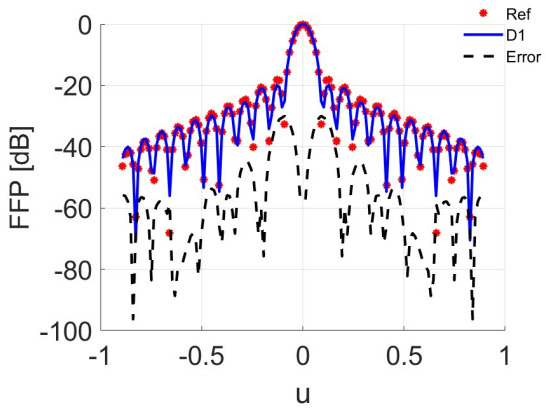

Figure 21: Reference FFP (red crosses), FFP reconstructed with D1 (blue line) and relative reconstruction error (black dashed line): PC along the cut for $v=0$, non-separable illumination, Case 2 - $d=15\lambda$.

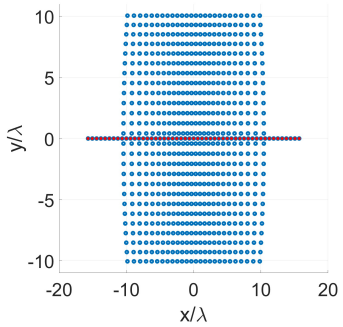

Figure 22: The sampling point distribution for Case 2, $d=5\lambda$ – D1 (red crosses), D2 (blue circles).

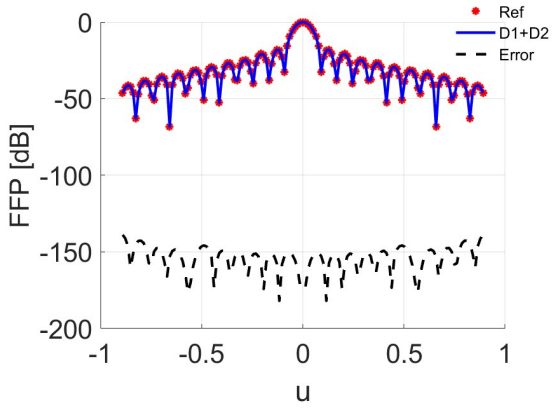

Figure 23: Reference FFP (red crosses), FFP reconstructed by using both D1 and D2 (blue line) and relative reconstruction error (black dashed line): PC along the cut for $v=0$, non-separable illumination, Case 2 - $d=5\lambda$.

The D2 measurement points are those strictly needed to get a satisfactory reconstruction of the FFP along the cut of interest. To highlight this key property of the approach, an inversion with few rows removed from D2 has been performed, showing a significant deterioration of the performance. In Fig. 24, the reconstruction obtained after removing 2 rows from the top and 2 from the bottom of the D2 distribution is presented with a dramatic increase of the error.

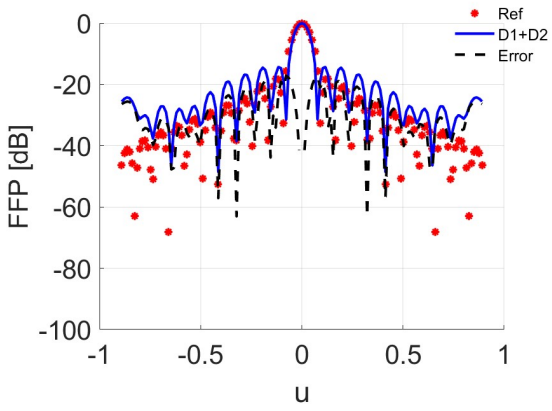

Figure 24: Reference FFP (red crosses), FFP reconstructed by using both D1 and D2 (blue line), with 4 rows removed, and relative reconstruction error (black dashed line): PC along the cut for $v=0$, non-separable illumination, Case 2 - $d=5\lambda$.

As a last case, a non-canonical radiator is considered. The antenna is able to radiate multiple beams thanks to the phase-only control applied at the sub-aperture level. It has a complicated, non-symmetrical, excitation which partitions the aperture into sub-apertures fed with a constant, controllable, phase. The design is reported in [18], which presents an optimal partitioning synthesis to reduce hardware complexity and control the undesired lobes levels due to quantization. Here the case of an aperture with size $15\lambda \times 15\lambda$, partitioned into 128 non-regular triangular sub-apertures, and radiating 3 pencil beams has been considered, and PC has been applied for the third beam in [18], i.e. when the beam pointing direction is (u, v) = (0,0.342).

The measurement distance d has been set equal to 10λ. The PC along the u=0 cut has been performed. SVO identifies the distribution D1 shown in Fig. 25 with 69 red crosses. Even if a large ε_{max} suggests the use of further points (D2 distribution), the reconstruction obtained by using D1 only is reported in Fig. 26 showing that, even in this complicated case, D1 allows a good identification of the main beam. To prove the agreement for the sidelobe, D2 has been considered. Its samples are reported in Fig. 25 as blue circles arranged in 44 non-uniformly spaced columns, made of 44 points each, non-uniformly spaced. To let the Reader appreciate the efficiency of sampling, we stress that the minimum spacing between two adjacent sampling points is greater than 0.7λ. In Fig. 27 the FFP evaluated after using D1 and D2 is presented, showing a dramatic improvement in the reconstruction of the sidelobes.

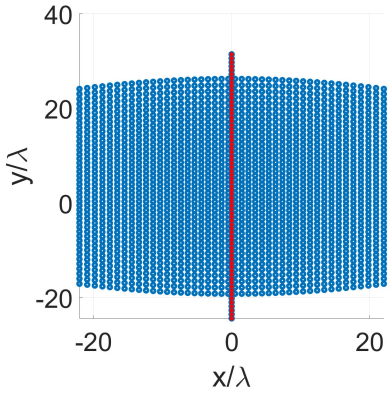

Figure 25: The sampling point distribution for the partitioned aperture case, $d=10\lambda$ – D1 (red crosses), D2 (blue circles).

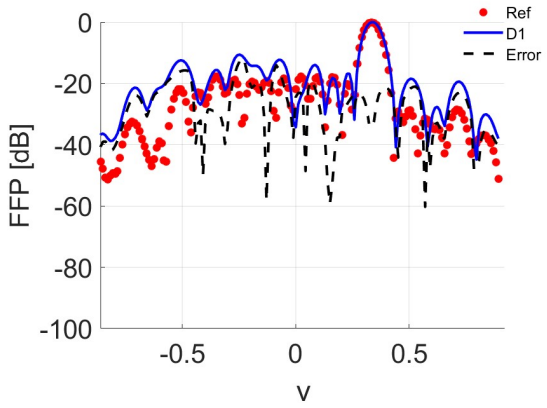

Figure 26: Reference FFP (red crosses), FFP reconstructed with D1 (blue line) and relative reconstruction error (black dashed line): PC along the cut for $u=0$, partitioned aperture case - $d=10\lambda$.

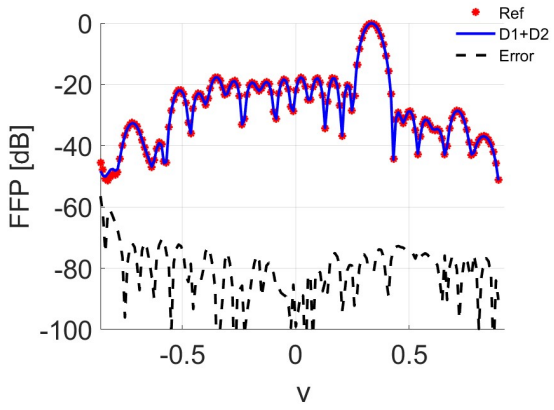

Figure 27: Reference FFP (red crosses), FFP reconstructed by using both D1 and D2 (blue line), and relative reconstruction error (black dashed line): PC along the cut for $u=0$, partitioned aperture case - $d=10\lambda$.

5. Conclusions

In this paper an approach for the PC that defines the general framework and highlights a strategy to define the optimal distribution of the NF samples needed to reconstruct the FFP along the cut of interest has been introduced, and the behavior of the reconstruction error has been parametrically analyzed. In particular, the attention has been focused on the reconstruction error achievable when PC in the fastest acquisition scheme, i.e. when using the distribution D1 only. A numerical analysis has been reported for several case studies, for separable and non-separable illuminations, parametrically as function of the measurement distance. The analysis shows coherent trends and highlights the differences depending on the excitations.

References

[1] A. Bangun and C. Culotta-López, "Optimizing sensing matrices for spherical near-field antenna measurements," *IEEE Trans. Antennas Propag.*, vol. 71, no. 2, pp. 1716–1724, Feb. 2023.

[2] F. D'Agostino, I. De Colibus, F. Ferrara, C. Gennarelli, R. Guerriero, and M. Migliozzi, "Far-field pattern reconstruction from near-field data collected via a nonconventional plane-rectangular scanning: Experimental testing," *Int. J. Antennas Propag.*, vol. 2014, pp. 1–9, Apr. 2014.

[3] A. Capozzoli, C. Curcio, A. Liseno, and P. Vinetti, "Field sampling and field reconstruction: A new perspective," *Radio Sci.*, vol. 45, no. 6, pp. 1–31, Dec. 2010.

[4] F. R. Varela, M. S. Castañer, F. Saccardi, L. Scialacqua, and L. Foged, "Planar wide mesh scanning using multiprobe systems," in *Proc. Antenna Meas. Techn. Assoc. Symp. (AMTA)*, Renton, WA, USA, Oct. 2023, pp. 1–5.

[5] M. Sierra-Castañer and S. Burgos, "Fresnel zone to far field algorithm for rapid array antenna measurements," in *Proc. 5th Eur. Conf. Antennas Propag. (EuCAP)*, Rome, Italy, 2011, pp. 3251–3255.

[6] T. Salmerón-Ruiz, M. Sierra-Castañer, F. Saccardi, S. Burgos, F. J. Cano-Fácila, and L. J. Foged, "A fast single cut spherical near-field-to-far-field transformation using cylindrical modes," in *Proc. 8th Eur. Conf. Antennas Propag. (EuCAP)*, The Hague, The Netherlands, 2014, pp. 2476–2480.

[7] R. Cornelius, T. Salmerón-Ruiz, F. Saccardi, L. Foged, D. Heberling, and M. Sierra-Castañer, "A comparison of different methods for fast single-cut near-to-far-field transformation," *IEEE Antennas Propag. Mag.*, vol. 56, no. 2, pp. 252–261, Apr. 2014.

[8] F. Rodríguez Varela, B. G. Iragüen, and M. Sierra-Castañer, "Undersampled spherical near-field antenna measurements with error estimation," *IEEE Trans. Antennas Propag.*, vol. 68, no. 8, pp. 6364–6371, Aug. 2020.

[9] F. Rodríguez Varela *et al.*, "Multi-probe measurement system based on single-cut transformation for fast testing of linear arrays," *Sensors*, vol. 21, no. 5, p. 1744, Mar. 2021.

[10] A. Capozzoli, C. Curcio, and A. Liseno, "Partial Near-Field antenna characterization," *IEEE Trans. Antennas Propag.*, vol. 72, no. 10, pp. 7448–7459, Oct. 2024.

[11] A. Capozzoli, C. Curcio, and A. Liseno, "Partial characterization of aperture antennas in planar near-field scanning," in *Proc. 19th Eur. Conf. Antennas Propag. (EuCAP)*, Stockholm, Sweden, 2025, pp. 1–5, doi: 10.23919/EuCAP63536.2025.10999772.

[12] F. R. Varela, B. G. Iragüen, and M. S. Castañer, "Single-cut phaseless near-field measurements using specialized probes," in *Proc. Antenna Meas. Techn. Assoc. Symp. (AMTA)*, Denver, CO, USA, 2022, pp. 1–5.

[13] F. R. Varela, A. Arboleya, C. Fontá, E. Martinez-de-Rioja, and J. C. Maeso, "Fast planar near-field measurements of reduced angular pattern domains," *IEEE Trans. Antennas Propag.*, doi: 10.1109/TAP.2024.3424515.

[14] A. Capozzoli, C. Curcio, G. D'Elia, and A. Liseno, "Singular value optimization in plane-polar near-field antenna characterization," *IEEE Antennas Propag. Mag.*, vol. 52, no. 2, pp. 103–112, Apr. 2010.

[15] A. Capozzoli, C. Curcio, and A. Liseno, "Different metrics for singular value optimization in near-field antenna characterization," *Sensors*, vol. 21, no. 6, p. 2122, 2021.

[16] A. Capozzoli, L. Celentano, C. Curcio, A. Liseno, and S. Savarese, "Optimized trajectory tracking of a class of uncertain systems applied to optimized raster scanning in near-field measurements," *IEEE Access*, vol. 6, pp. 8666–8681, 2018.

[17] A. Capozzoli, C. Curcio, and A. Liseno, "Truncation in "Quasi-Raster" Near-Field acquisitions [Measurements Corner]," *IEEE Antennas Propag. Mag.*, vol. 54, no. 5, pp. 174–183, Oct. 2012.

[18] A. Capozzoli, C. Curcio, G. D'Elia, and A. Liseno, "A technique for the array partitioning," *Radio Sci.*, vol. 57, no. 10, pp. 1–22, 2022.